Article:

Liu, K, Boardman, R, Mavrogordato, M et al. (2 more authors) (2020) The Importance of the Heel Effect in X-Ray Ct Imaging of Soils. Environmental Geotechnics. pp. 1-15. ISSN 2051-803X

https://doi.org/10.1680/jenge.20.00048

THE IMPORTANCE OF THE HEEL EFFECT in X-RAY CT IMAGING of SOILS

K. Liu[1], R. Boardman[2], M. Mavrogordato[3], F. A. Loveridge[4] *, and W. Powrie[5]

*** corresponding author (f.a.loveridge@leeds.ac.uk; 07773346203)**

ABSTRACT

Non-destructive and non-invasive X-ray computed tomography (CT) is increasingly used in environmental geotechnics research. As a result of recent advances in technology and image processing techniques, CT with rapid scanning now has the potential to track changes in soil structure or soil water conditions as they happen, rather than as previously on a specimen in (temporary) stasis. Gathering meaningful data in a short scan time requires compromises to be made on parameters such as exposure time, and / or the use of higher X-ray intensities and energies. Data processing and imaging processing - including the removal of any artefacts, which can cause errors in interpretation of soil structure or phase proportions - then become especially important. One such artefact is the heel effect. It has been recognised in medical imaging, owing to its association with high scan energies. However, it has not previously been identified in soil imaging, despite the trend towards using higher energies. This paper presents an investigation into the potential for the heel effect to affect the soil property determination. It is shown for the first time that a noticeable heel effect will be present in CT images of soils and derived phase proportion data, when certain types of X-ray reflection targets are used. A correction method for the heel effect is presented, use of which will prevent significant errors in derived soil parameters such as water content.

Word Count

Abstract: 231 words

Main text: 7257

Keywords

Computed tomography, Laboratory tests, Soil structure, Soil characterisation, Heel effect

Notation:

CT computed tomography

[1] Faculty of Engineering and Physical Sciences, University of Southampton, Southampton, SO17 1BJ, UK; 0000-0002-7533-1272

[2] Faculty of Engineering and Physical Sciences, University of Southampton, Southampton, SO17 1BJ, UK; 0000-0002-4008-0098

[3] Faculty of Engineering and Physical Sciences, University of Southampton, Southampton, SO17 1BJ, UK; 0000-0002-3956-2866

[4] Faculty of Engineering and Physical Sciences, University of Leeds, Leeds, LS2 9JT, UK; 0000-0002-6688-6305

[5] Faculty of Engineering and Physical Sciences, University of Southampton, Southampton, SO17 1BJ, UK; 0000-0002-2271-0826

GV	grey value
ROI	region of interest

1 INTRODUCTION

X-ray computed tomography (CT) is increasingly used for research in soil mechanics, geotechnical engineering and soil science. The technique involves passing X-rays through a soil specimen mounted on the manipulator and measuring the arrival of photons at the X-ray detector. Repeating this procedure for many angles of incidence as the specimen rotates generates a series of 2D radiographs, one for each angle. This enables a three dimensional model to be built up that provides information on density contrasts according to the differential absorption of the photons at the specimen. The density information can then be used to identify the soil phases, soil structure (e.g. Sleutel et al, 2008) and other geotechnical parameters including incremental strain from applied loading (e.g. Ando et al, 2012a, b).

The approach has become popular as a method for non-destructive and non-invasive examination of soil specimens in at least a temporary state of stasis. However, advances in technology and image processing techniques mean that X-ray CT is increasingly being seen as a way to track and meaningfully quantify changes in soil structure or changes in soil water conditions as they happen with time (e.g. Cnudde & Boone, 2013), enhancing its utility in environmental geotechnics. Applications in environmental geotechnics are varied and diverse and include for example reservoir characterisation (Van Geet et al, 2000), soil water retention characterisation (Khaddour et al, 2018), measurement of liquid and/or gas flow and associated deformation (Mees et al, 2003, Alvarez-Borges et al, 2018, Wang et al, 2019), quantification of soil-biological interactions (Helliwell et al, 2013). To track changes in soil phases or structure with time, the associated rapid scanning processes require a careful balance between speed and quality. Minimising the scan duration ensures that temporal changes are captured and images are not blurred, for example due to a significant changes in water content within the specimen or specimen movement during a single scan. At the same time, it is important to maintain the image quality traditionally associated with a longer scan time. This means that compromise on some scan settings may be required, for example using shorter exposure times or a smaller number of projections in combination with higher X-ray intensities and energies.

If scan setting compromises lead to a lower resolution CT image, different soil phases may occur within the same image voxel. This is known as the partial volume effect (Ketcham 2005). To avoid errors arising from averaging of phase densities within voxels, data processing to remove artefacts become especially important. Artefacts or anomalies in the data obtained may cause deterioration in image quality and reduce the accuracy of image analysis, including parameters such as soil phase proportions (e.g. porosity, water content), which can be derived by segmentation.

Common artefacts that can hamper reliable image segmentation include beam hardening and rings (Boas & Fleischmann, 2012, Ketcham & Hannah, 2014). Beam hardening is a limitation arising from polychromatic X-ray sources (Ketcham and Carlson, 2001), in which there is selective attenuation of lower energy photons. This can cause dark streaks in images where there is greatest attenuation, or a “cupping” artefact, where an artificially bright zone is present around the edges of a specimen. Beam hardening can be easily addressed by filtration of the X-ray beam before it reaches the specimen. A ring artefact is a dark ring, centred about the specimen rotation point; it results from a deficiency in the X-ray detector and is a systematic error (Davis and Elliott, 2006). Rings are usually removed by calibration of the detector, or by moving the specimen or detector by a small, subsequently-corrected, random amount between frames.

The artefact known as the heel effect is associated with CT scanning systems in which the incident X-rays are generated by means of a reflection target. It has been recognised in medical imaging due to its association with high scan energies. However, it has not been previously identified in soil imaging. The trend in soil mechanics towards more sensitive contrast differentiation from X-ray CT images (e.g. Liu et al, 2017, Alvarez-Borges et al, 2018, Liu, 2020) places the scan energies utilised into a similar category to biomedical imaging. This brings the potential for an undetected and / or uncorrected heel effect leading to errors in image interpretation and derived parameters, for example changes in water content associated with thermal or chemical processes, or changes in soil density related to mechanical loading.

This paper presents the first investigation into the potential for the heel effect relevant to soil imaging. First, we review the heel effect artefact and recent trends of increasing scan energy in applications of X-ray CT to problems in soil mechanics. Then we identify the presence of the heel effect in soil and control materials, before investigating which factors influence the magnitude of the effect. Finally, we assess methods to avoid errors arising from the heel effect, and propose a new universal correction method to remove the artefact.

2 BACKGROUND

2.1 The Heel Effect

CT scanners use targets between the electron beam source and the object being scanned to generate X-rays in a pattern suitable for imaging. These targets are generally of either the reflection or the transmission type (Figure 1). Reflection targets are more commonly used in laboratory microfocus

X-ray CT sources. The heel effect is an image artefact that results from the inherent features of a reflection type target.

Reflection targets are usually formed of inclined metallic plates (Figure 1a). They are frequently adopted in high energy applications as they are easily cooled and provide good flux. Electrons generated by a hot tungsten filament (cathode) are accelerated to the target (anode), where interactions occur at an atomic level to produce X-rays that are emitted onto the detector. Owing to the angle at which the target is set, the emerging X-rays will pass through more of the target material on the downslope side than on the upslope (Figure 1a). Some of the X-rays will be attenuated more significantly by the extra thickness of the target material. This is because as the thickness of a given material increases, the chance of a photon of a given energy being absorbed increases according to the Lambert-Beer law (Swinehart, 1962). X-ray paths with different reflection angles will therefore experience correspondingly different degrees of filtration. Hence in the example shown in Figure 1a, the resulting projection will tend to reduce in intensity with decreasing vertical elevation. This will cause a gradient in the distribution of the grey value (GV), a measure of specimen density, evaluated at the detector. This is known as the heel effect.

The heel effect is often slight and may not significantly affect some types of image analysis - for example, where there is no particular interest in the spatial distribution of a soil property. Owing to the origin of the heel effect in the attenuation of photons, it will be more noticeable in scans where high energies are used. This has typically included medical applications, but is also now starting to include geotechnics as discussed in Sections 2.2 and 2.3 below.

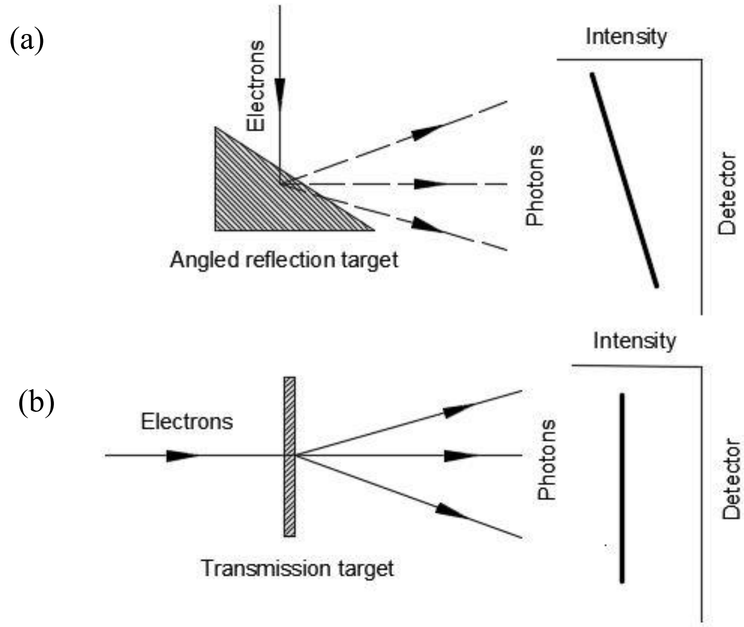

Figure 1: Schematics of X-ray (a) reflection target and (b) transmission target

As an alternative to a reflection target, a transmission target may be used. This is placed perpendicular to the electron beam (Figure 1b). X-rays are generated within a small region of substantially uniform thickness, and penetrate directly through the thin target material. Thus the intensity of the resulting X-rays is theoretically uniform and transmission targets do not show the heel effect.

2.2 The Heel Effect in Medical Applications

The heel effect was initially identified in the medical field, as medical CT scanners normally use reflection targets owing to the high flux required for the rapid scanning of large objects (patients). Several correction or compensation methods have been proposed. A method using a compensation filter (where the aluminium layer of either side of the target is increased in thickness on one side) was developed by Mori et al, 2005, to eliminate potential radiation damage to patients. Heel effect corrections based on simple first-order beam hardening (Braun et al, 2010), and a slice-by-slice background subtraction approach (Johnston et al, 2015) have also been proposed. However, these approaches have limitations in that their application requires detailed understanding of the target composition and geometry, hence additional specialist input.

2.3 High Energy X-Ray CT Scanning in Soil Mechanics

The heel effect will be present in all scans carried out using a reflection target. There is no threshold energy above which the effect should be noticeable, as this will be a function of the image contrast. Nonetheless, it is expected that higher energies would lead to a more pronounced heel effect. In this section, we review recent soil scanning applications that have used higher energies.

CiSlerova et al (2002) used a medical CT scanner (Siemens SOMATOM PLUS IV) to scan soil specimens with a peak scan energy of 140 kV; Farber et al (2003) used a Skyscan 1072 high-resolution X-ray micro-tomography unit (Skyscan, Belgium) to study the porosity of granules; and Taud et al (2005) used a peak scan energy of 130 kV on a PICKER IQ PREMIER (IQXTRA) scanner to explore porosity in a rock. The energy values in all these studies are within or above the range shown in this paper to cause a noticeable heel effect. However, none of these studies considered the spatial distribution of specimen density, porosity etc., so any errors potentially present due to the heel effect would remain unnoticed.

Some studies have derived spatial distributions of density or density related parameters without explicitly identifying the influence of the heel effect. For example, Andesron et al (1990) used a Siemens SOMATOM DR Version H scanner with a peak energy of 125 keV to analyse macropores in undisturbed soil cores. They evaluated bulk density distributions in soil cores scanned horizontally. Otani et al (2010) correlated overall material density directly with CT grey value following 150 kV peak energy scanning of fine to coarse Yamazuna sand, and used the results to identify shear zones. Density changes in shear zones were also assessed by Desrues (2004) for fine sand scanned using a ND8000 medical scanner. Derived void ratio values were reported, but not their spatial distribution. Alvarez-Borges et al (2018) examined changes in chalk density following model pile penetration using a modified 225 keV Nikon/Xtek HMX device. Scan energies were 200 keV, and the resulting images interpreted using a GV density calibration.

Alshibli & Hasan (2008) analysed the porosity of a medium sand specimen before and after shearing, using a MSFC CT facility with a peak scan energy of 335 kV. A fairly uniform distribution of void ratio was obtained within their specimen before compression, based on the void ratio map of a centre section. Fonesca et al (2013) reported differences between void ratios in medium sand determined by gravimetric measurement and X-ray CT scans (using a micro-CT scanners, developed by phoenix|X-ray (GE)) of between 9 % and 25 %. They attributed the differences to the heterogeneity of the specimen reducing the accuracy of comparisons between global gravimetric data with the local values determined by CT scanning, and did not explicitly consider the possibility of the heel effect.

These studies show that it is possible to scan soil specimens at high energies and not experience the heel effect. This could be due to one of a number of reasons, including the nature of the soil properties determined from the analysis; the highly localised nature of the results obtained; other sources of error obscuring the effect; or it simply having gone unnoticed and uncorrected. We will show in this paper that manifestation of the heel effect depends on energy levels and soil grain size;

hence it may be that the materials in these studies were coarse relative to the energy levels used. In such cases, the individual grains may be distinguishable directly so that the phase proportions can be calculated without error. Given these uncertainties, it is important to demonstrate that the heel effect can be non-negligible in soil imaging. Awareness of the artefact can then guard against future error as soil scan energies increase further.

3 EXPERIMENTAL APPROACH

A comprehensive programme of experiments was carried out to demonstrate the presence of the heel effect in soil imaging and understand the importance of different factors influencing the magnitude of the artefact. Three different types of specimen were used; first, empty acrylic specimen containers comprising two homogeneous phases (acrylic and air) that were not susceptible to the preparation-induced variability that may occur with real soils. This allowed initial carefully controlled experiments to be carried out to confirm the presence of the heel effect in the scanners utilised, in ideal conditions without internal specimen variability.

Secondly, granular materials were used to assess the presence of the heel effect in images of soils, and to show the effect of different grain sizes on the magnitude of the artefact. Leighton Buzzard sand was used for this purpose, as it is well known and understood. Different particle sizes were tested, from Fraction B to Fraction E. The third material tested was a clay - London Clay was used, again because its properties are well-known.

3.1 Materials

Purpose-built circular cylindrical containers, of internal diameter 5mm, 8mm and 20mm and corresponding height 10mm, 20mm and 50mm respectively, were made by 3D printing. The containers were scanned empty or containing soil specimens.

Leighton Buzzard sand specimens of different grain sizes (Table 1) were prepared by air pluviation directly into the containers. Most of the specimens were prepared dry to allow the simplest initial assessments. However, wet pluviation was also used with some specimens to facilitate comparison with the London Clay, which could not be used dry. London Clay specimens were prepared by slurry deposition.

Table 1: Grain Sizes of Soil Materials

	Leighton Buzzard sand				*London Clay*
	LB-B	*LB-C*	*LB-D*	*LB-E*	
Descriptor	Coarse sand	Medium sand	Fine to medium sand	Fine sand	Silty clay or Clay
Range of mean grain size(μm)	1180 – 600	600 – 300	300 – 150	150 – 90	1 * <5 **
% coarser than range	10	10	10	15	NA
% finer than range	10	10	15	15	NA

* Zhang et al, 2016; ** King (1991)

3.2 Scanning

Four different X-ray CT scanners in the University of Southampton μ-VIS X-ray Imaging Centre (University of Southampton, 2017) were used for the experiments. Initially the Nikon HMX ST 225 (designated "HMX"), Nikon/Metris custom Hutch (225kV peak modality) ("Hutch") and Zeiss Xradia Versa 510 ("Versa") scanners were used to confirm the presence of the heel effect. Each of these machines has a different X-ray target (Table 2) and hence were expected to show different results with respect to the heel effect. After these initial confirmation scans, a range of sensitivity experiments related to the heel effect were carried out using the Nikon/Metrix CT Benchtop 160 Xi machine ("Benchtop"), which has a vertical reflection X-ray target.

Table 2: Features of various scanners (see University of Southampton (2017) for more details)

CT Scanner	*Short name in text*	*Target source*	*Expected heel effect*
Nikon/Metrix CT Benchtop 160 Xi	Benchtop	Reflection target mounted vertically	Vertical
Nikon HMX ST 225	HMX	Reflection target mounted vertically	Vertical
Nikon/Metris custom Hutch (225kVp modality)	Hutch	Reflection target mounted horizontally	Horizontal
Zeiss Xradia Versa 510	Versa	Transmission target	None

The materials and scan settings used for all the experiments are given in Table 3. The scan settings are defined by the energy, which affects image contrast; the power and exposure time, which controls the number of X-ray photons; the projection count, which ensures the intactness of the image features; and the number of frames per projection, which is chosen to minimise movement artefacts and reduce noise. Overall, the settings were chosen to maximise image quality within the constraint of scan time during which the state of the specimen would not change significantly – a key factor when the specimen is not in stasis. Of the scan parameters, only the scan energy would be expected to influence the magnitude of the heel effect observed. Taking the first row of Table 3 as an example, two frames per projection at 500 ms exposure means that every projection is made up of the mean of two acquired images, each exposed for 500 ms. Consequently, the total exposure time per projection is 1000 ms.

The confirmation scans were carried out on 5mm diameter specimen containers, either empty or filled with Fraction E Leighton Buzzard Sand. These experiments were designed to show the difference between the horizontal and vertical reflection targets in the Hutch and HMX machines, and the presence or absence of the heel effect in the soil specimens in the HMX and Versa machines, the latter of which uses a transmission target.

Subsequently, empty pots were used to assess the influence of scan energy on the magnitude of the heel effect, and any impact of specimen size for a given set of scan settings. In this case, the resolution changes according to the specimen size (Table 3). Finally, soil specimens of different grain sizes and saturations were tested, again at the same scan settings.

Table 3: Experiment Details and Scan Settings

Purpose	*Container Size Dia/Ht (mm)*	*Specimen*	*Scanner*	*Peak Energy kV*	*Power W*	*Exposure ms*	*Frames per projection*	*Projection count*	*Resolution μm*
Confirm presence of heel effect	5/10	Empty	HMX	75	7	500	2	3142	5.8
	5/10	Empty	Hutch	75	7	500	1	1601	6.3
Confirm presence of heel effect in soils	5/10	LB-E dry	HMX	85	7	500	1	3142	3.9
	5/10	LB-E dry	Versa	85	7	4	1	3201	5.7
Demonstrate effect of scan energy	5/10	Empty	Benchtop	60	6	1067	4	1905	10.4
	5/10	Empty	Benchtop	80	6	1067	4	1905	10.4
	5/10	Empty	Benchtop	100	6	1067	4	1905	10.4
	5/10	Empty	Benchtop	120	6	1067	4	1905	10.4
	5/10	Empty	Benchtop	140	6	1067	4	1905	10.4
Investigate effect of absolute specimen size	5/10	Empty	Benchtop	80	7.5	534	4	1000	9.1
	8/20	Empty	Benchtop	80	7.5	534	4	1000	17.3
	20/50	Empty	Benchtop	80	7.5	534	4	1000	43.2
Investigate effect of soil grain size and saturation	5/10	LB-B dry	Benchtop	100	6	1067	4	1905	9.5
	5/10	LB-C dry	Benchtop	100	6	1067	4	1905	9.5
	5/10	LB-D dry	Benchtop	100	6	1067	4	1905	9.5
	5/10	LB-E dry	Benchtop	100	6	1067	4	1905	9.5
	5/10	LB-E saturated	Benchtop	80	6	1067	4	1905	9.5
	5/10	London Clay saturated	Benchtop	80	6	1067	4	1905	9.1

3.3 Data Processing

3.3.1 Image Reconstruction

During scanning, the specimens were rotated and radiographic projections ("X-ray images") taken with an equiangular spacing of 360 degrees divided by the projection count. The raw data were then reconstructed using vendor-specific implementations of the Feldkamp Davis Kress algorithm (Feldkamp et al, 1984) in Nikon X-TEK CT Pro 3D (Version XT 2.2 Service Pack 11), to provide a stack of 2D horizontal plane images together giving a representation of the 3D image. The stack of images was used to evaluate the vertical heel effect using the grey value (GV) and derived porosity distributions.

To evaluate the heel effect in the horizontal plane (when using the Hutch machine), the GV was measured directly using the original 2D radiographic projections, before any reconstruction was carried out. This is because reconstruction reduces the magnitude of the horizontal heel effect when the reflection target is arranged horizontally. In this specific case, the artefact is largely averaged out between reciprocal projections in radiographs oriented at 180 degrees.

3.3.2 Image Processing and Thresholding

After reconstruction, image processing for each soil specimen was limited to a region of interest (ROI) centred on the axis of the specimen, to eliminate boundary or edge effects. Analyses of empty specimen containers focused on small regions of the acrylic wall.

For the larger image data from the HMX, Hutch and Versa machines, the GV range of each image stack was scaled to enhance the contrast between the different phases. Before further image processing, the reconstructed raw image data were converted into 8-bit unsigned integer format to reduce the computing time. Analysis of the relatively smaller image data from the Benchtop scans was based on the raw 32-bit floating point data. For greyscale featured image data, a lower GV corresponds to less dense and a higher GV to denser material. For example in an 8-bit integer image, the range of greyscale is between 0 (completely "black") and 255 (completely "white"), representing the least and the most dense materials, respectively. For presentation of some images in this paper, contrast enhancement was applied to help illustrate the heel effect.

For quantitative assessment of the soil phase relationships, the scan data were thresholded to differentiate the sand grains from the voids based on their density, as reflected in their GV. In demonstrating the presence of the heel effect and presenting the results of the sensitivity analysis (in Sections 4 and 5 respectively), the primary method of thresholding used is the Otsu method (Otsu, 1979). This popular method was chosen because it is simple and straightforward to apply, has a very fast analysis time (in the order of seconds), and is robust as it does not require the selection of additional fitting parameters. The approach searches for the threshold that minimises the intra-class variance based on the shape of the overall GV intensity histogram, and has been shown to work well for two phase soil systems (e.g. Watanabe et al., 2012; Zhao et al, 2015) where there is sufficient contrast between those phases. In Section 6, the Otsu method is compared with more sophisticated adapted thresholding methods (e.g. Bernsen, 1986; Niblack, 1986) offering a possible way of removing the heel effect artefact.

4 DEMONSTRATION OF THE HEEL EFFECT

4.1 Vertical Heel Effect

Four regions of similar area at different orientations on the empty specimen container were investigated (Figure 2a). As the density of the acrylic container was homogeneous, the GV distribution should have been uniform. However, a marked gradient is apparent in the vertical direction (Figure 2a) for the data gathered using the HMX. In contrast, the vertical distribution of GV obtained using the Hutch is uniform when shown at the same scale (Figure 2b). This confirms the presence of a vertical heel effect in the HMX scanner and the absence of the vertical heel effect in the Hutch machine, which is equipped with a horizontal reflection target.

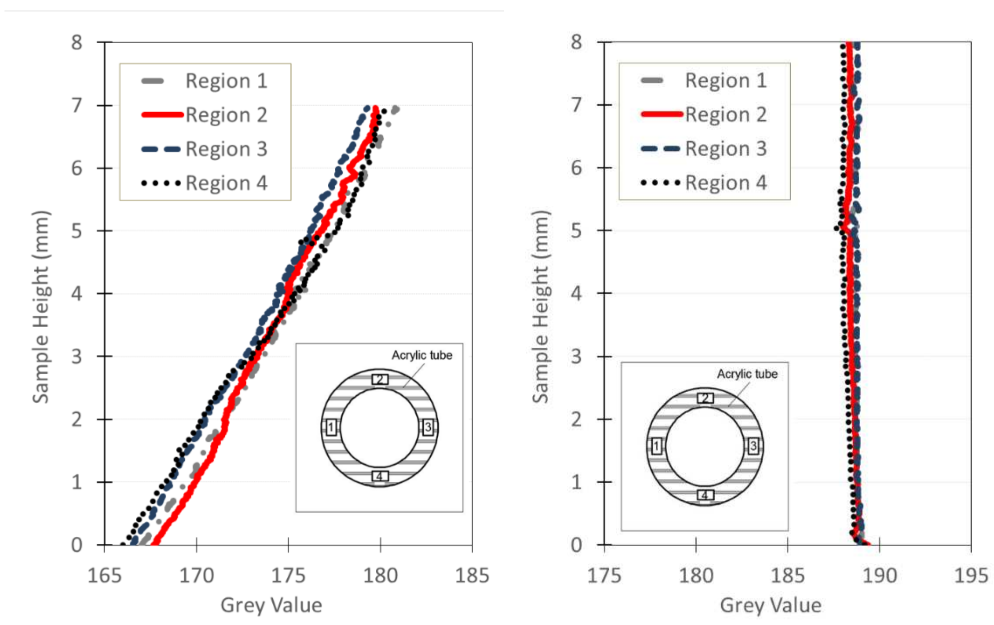

Figure 2: Grey value (GV) distribution of the specimen container acrylic wall from (a) the HMX with vertical reflection target and (b) the Hutch with horizontal reflection target.

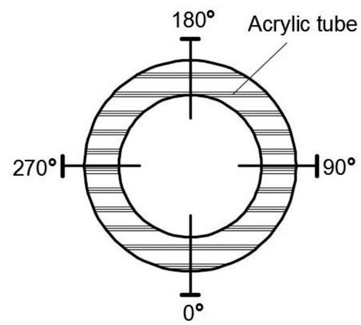

Figure 3: Sketch of the 2D slice showing the projections at four orthogonal angles

4.2 Horizontal heel effect

Four mutually orthogonal radiographs (at $\theta = 0^{\circ}$, 90°, 180° and 270°; Figure 3), over a 3 mm height positioned above the horizontal centreline, were used to assess a potential horizontal heel effect. The plots in Figure 4 show the GV profile for the ROI in each projection as a function of the distance along the projection (in pixels). In each case, the GV for the air phase is high in the centre of the plot, then falls where the projection intercepts the acrylic wall of the container. The GV reaches a minimum at the internal boundary of the wall, and increases when the air phase outside the container is reached. In the absence of the heel effect, each radiograph would be expected to show reasonable symmetry.

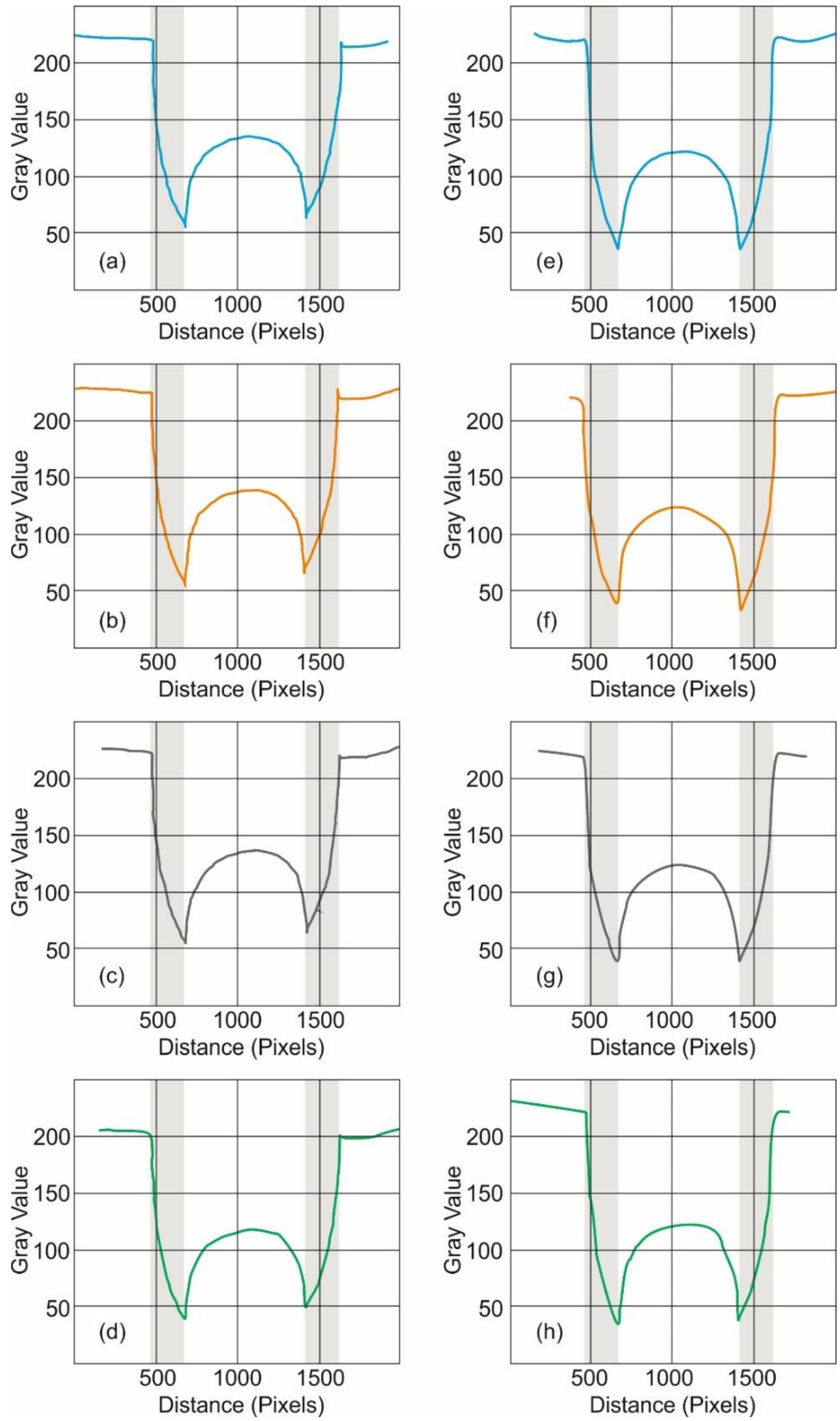

Figure 4: Grey value profiles for the ROIs from four orientations: (a) 0° (b) 90° (c) 180° (d) 270° using data from the Hutch machine with horizontal reflection target; (e) 0° (f) 90° (g) 180° (h) 270° using data from the HMX machine with vertical reflection target. The shaded regions represent the acrylic wall of the specimen containers.

In the Hutch results (Figure 4a to Figure 4d), the minima on the left are always lower than those on the right, regardless of the orientation of the scan. This is a manifestation of the horizontal heel effect. In comparison, the HMX data (Figure 4e to Figure 4h) show a much more consistent result. In Figure 4e and Figure 4g, the left hand minima are the same as those on the right. This is because (e) and (g), and (f) and (h) (and also (a) and (c), and (b) and (d)) are pairs of mirror projection images at the same orientation. The consistency of these pairs demonstrates that the horizontal heel effect is not present in the HMX.

4.3 The Heel Effect in Sand

4.3.1 Effect on Grey Value

A specimen of dry Fraction E Leighton Buzzard sand in a 5mm diameter container was used to assess the implications of the heel effect for imaging in soils. The HMX (vertical reflection target) and Versa (transmission target) machines were used. To avoid the influence of cone-beam artefacts (Zbijewski & Beekman, 2006; Hsieh et al, 2007) and reduce computing time, a section about 4 mm in height around the middle of a 10 mm sand specimen was selected for analysis. Figure 5 shows the resulting orthogonal images from the two scans, as originally processed (Figure 5a, c) and with contrast enhancement (Figure b, d). The contrast enhancement reveals the vertical heel effect as a gradient in greyscale. In Figure 5c there is a clear top to bottom darkening of the image from the HMX. This effect is not noticeable with Versa.

Taking a slice from the HMX dataset at mid height and near the base (Figure 6) shows clearly how the heel effect has effected the GV. Figure 6c also includes the GV histogram for the ROI in each of the two slices. The two phase peaks are both shifted to the left in the lower darker slice; and in addition, the overall range of GV is also reduced. This has implications for thresholding as a reduced range may make it harder to separate phases. This is discussed below and in Section 5, where the impact of specimen grain size is investigated.

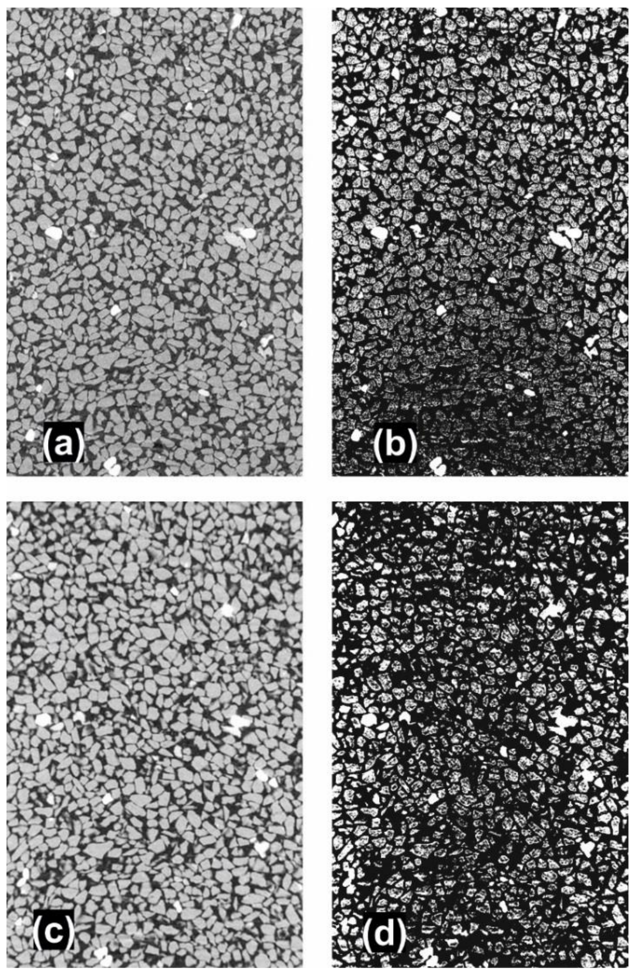

Figure 5: Orthogonal images for dry Fraction E Leighton Buzzard sand a) scanned using the HMX; b) scanned using the HMX with contrast enhancement, c) scanned with the Vera; d) scanned with the Versa with contrast enhancement

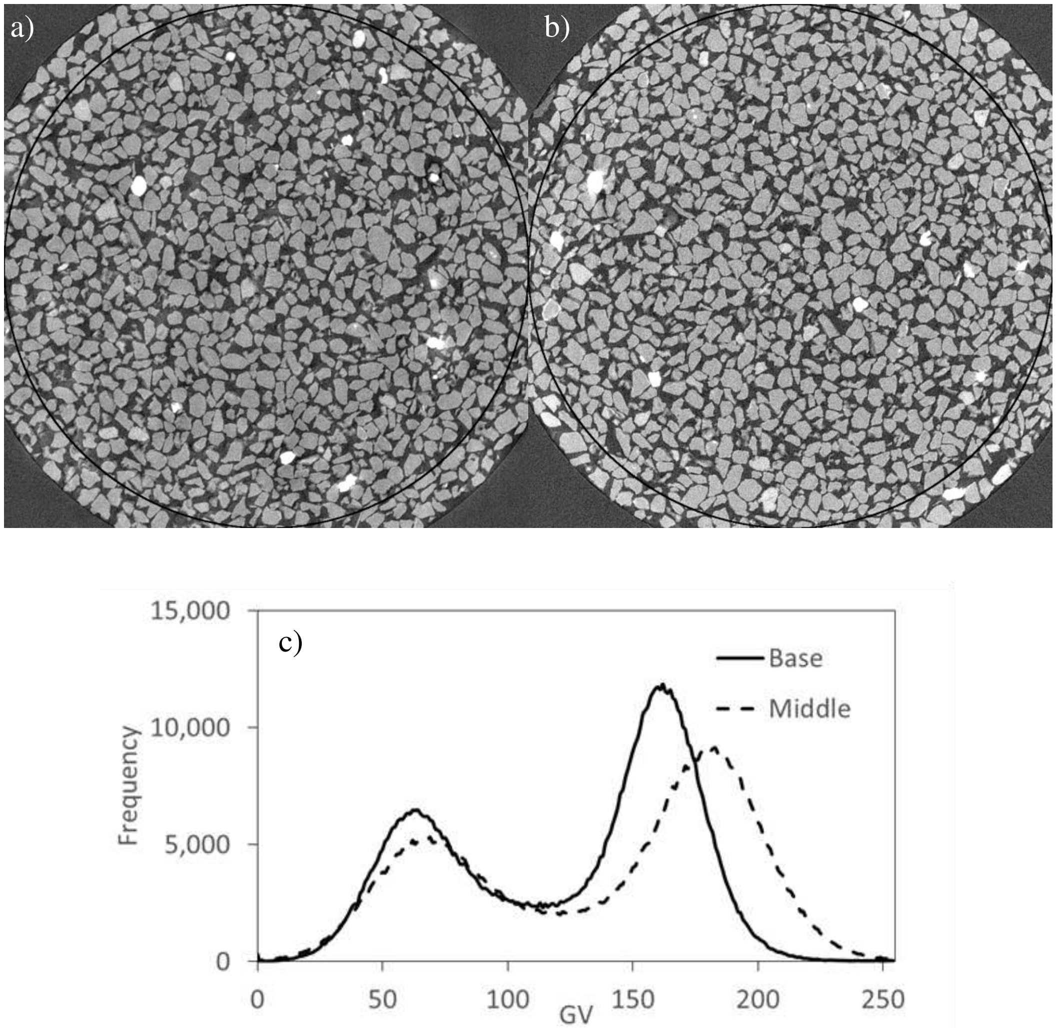

Figure 6: Processed CT images for Fraction E Leighton Buzzard sand taken from the HMX for: a) a slice near the base; b) a slice near the centre of the specimen; c) GV histograms for the ROI in the two slices.

4.3.2 Effect on Thresholding and Phase Determination

The magnitude of the heel effect may be quantified. Instead of working in terms of grey value (as in Sections 4.1 and 4.2 when considering only the specimen container), in this case the scan data were thresholded to determine the phase proportions. Data were processed using both global thresholding and local individual slice thresholding. Global thresholding is applied to each image slice based the GV thresholds determined from the overall GV intensity histogram for the entire specimen. In individual slice thresholding, each image slice is assessed with reference to the GV thresholds determined from its own GV intensity histogram. Comparison of the results of the two thresholding approaches can be used to evaluate the influence of the heel effect. Figure 7a shows that with global thresholding, the data obtained using the HMX exhibit an apparent reduction in porosity of about 5 % over the imaged specimen height (4 mm ROI). In contrast, the Versa data (Figure 7b) show a uniform distribution of porosity with a variation of less than 1 % over the same length scale.

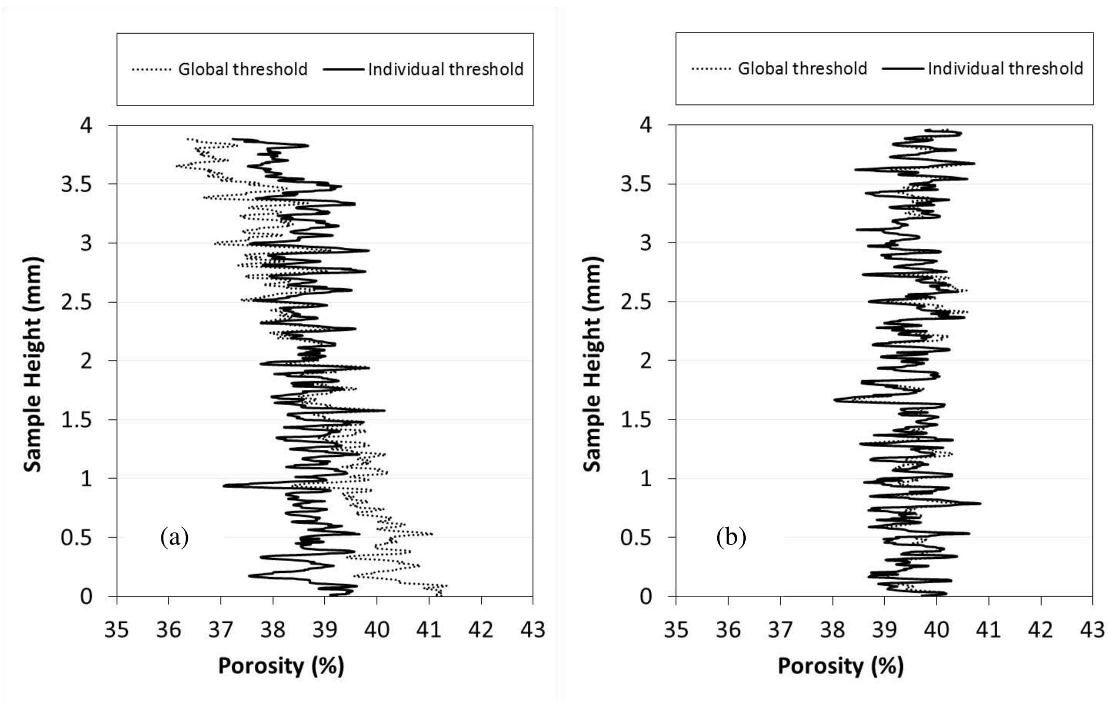

Figure 7: Porosity distributions from (a) HMX and (b) Versa scans of a 5 mm diameter dry Fraction E Leighton Buzzard sand specimen

The apparent decrease in porosity with height shown by the HMX is an artefact resulting from the increasing gradient of the GV distribution caused by the vertical heel effect. It is shown later that the degree of error introduced by the heel effect (about 5 % in this case) can be affected by the applied energy and the extent of the partial volume effect.

In contrast, the porosities determined using individual thresholding are uniform (Figure 7a). While this may at first sight seem to offer a suitable way of correcting for the heel effect, making reference to only the GV data from each slice without knowledge of the remainder of the data sets leaves the process open to errors and the potential to fail to identify real height dependent trends. For example, when applying individual thresholding, a small number of high density grains could cause the threshold value to be chosen at a GV range adequate for these particles but inappropriate for the remaining grains. A similar effect could occur with partial saturation. Hence individual thresholding is not recommended in practice. Individual thresholding is also more computationally expensive that global thresholding, and is not always possible in cases with a strong partial volume effect, where the GV must be calibrated for density or other techniques applied (e.g. see Liu et al, 2017). Since global thresholding is also a more common approach in practice, this means that the heel effect may be important in geotechnical analysis for certain scan settings and soil specimen conditions. The magnitude of this effect and how it may be countered are discussed in Sections 5 and 6 respectively.

The overall global porosity of the specimen was also determined from the HMX and Versa data (Table 4). These results are consistent, with a variation of less than 1 %. Thus the heel effect seems mainly to influence the apparent distribution of the specimen density, rather than the overall value. This is another reason why the effect may not have been noticed in previous research (see Section 2.3). In the present case, the overall porosity determined from gravimetric data was 39.3 %, which is in close agreement with the CT data.

It can therefore be concluded that the heel effect exists independently of specimen materials. If a reflection target is used in soil scanning, the artefact will influence the resulting image analyses of geotechnical phase relationships where knowledge of the spatial distribution is required. The heel effect can only be prevented directly by avoiding the use of reflection targets, especially those oriented vertically.

Table 4: Overall porosity from HMX and Versa scans of a 5 mm diameter dry Fraction E Leighton Buzzard sand specimen

Porosity (%)	*HMX data*	*Versa data*	*Corrected HMX data*
Otsu global threshold	38.8	39.6	38.9
Otsu individual threshold	38.6	39.5	38.8
Adaptive threshold (Bernsen)	38.4		
Adaptive threshold (Niblack)	38.6		
Gravimetric measurement		39.3%	

5 RESULTS OF SENSITIVITY ANALYSIS

5.1 Influence of Scan energy

As the heel effect is related to X-rays, energy is a key parameter and the heel effect is expected to be greater at higher energies. This was demonstrated by scans of an empty 5 mm internal diameter acrylic specimen container. Five different peak scan energies (60 kV, 80 kV, 100 kV, 120 kV and 140 kV) were applied using the Benchtop machine. Three scans were carried out for each energy level, giving fifteen scans in total. Four ROIs on the acrylic wall of the container from each set of data were used for analysis. The mean gradient of the four GV curves was determined in each case, with the average of the results from the three scans at the same energy being taken as representative. The analysis was based on the raw 32-bit data to avoid potential inconsistencies arising from data conversion. 800 slices without any cone-beam artefacts were selected for the analysis of the gradient of GV distribution.

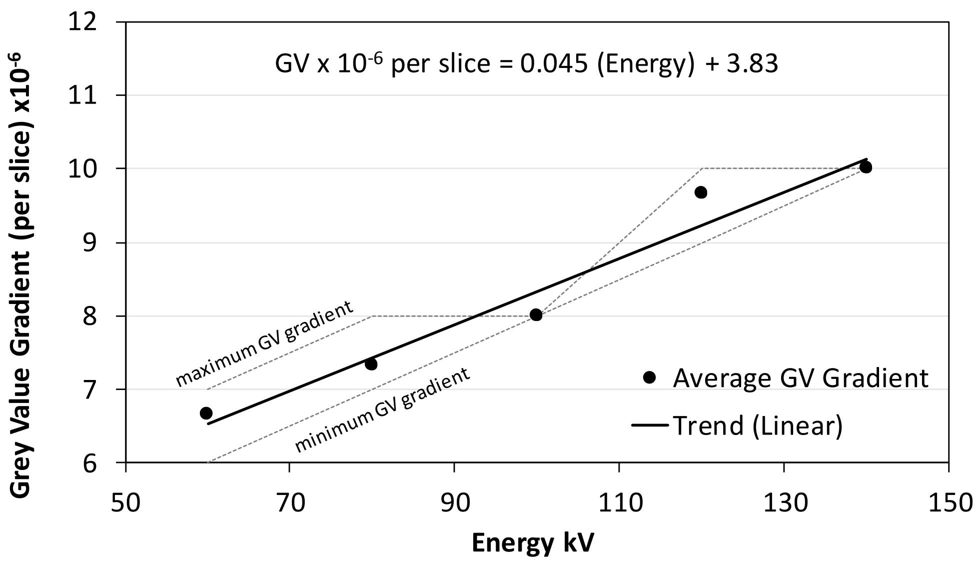

Figure 8: Average and range of grey value gradients for a 5mm internal diameter specimen container using different scan energies in the Benchtop machine.

The grey value gradient induced by the heel effect is plotted against the scan energy in Figure 8, in which the data points represent the average gradient for each energy, the solid line is the trend, and the dashed lines give the minimum and maximum GV gradients determined. As expected a positive linear relationship is obtained. This is because as the scanning energy increases, the X-rays will penetrate deeper into the target material with more generated photons being attenuated, causing a wider GV magnitude range to be reflected on the X-ray detector. In this case doubling the scan energy results in 145% of the initial GV gradient.

5.2 Influence of Specimen size

To assess the effect of specimen size on the heel effect, empty acrylic containers having internal diameters of 5 mm (10 mm in height), 8 mm (20 mm in height) and 20 mm (50 mm in height) (with a wall thickness of 1 mm in each case) were scanned under the same imaging conditions and with the same scan settings (Table 3). When the containers were scanned, they filled entirely the field of view of the radiograph. This means that larger containers were scanned to a correspondingly lower resolution, with the container wall represented by fewer voxels.

Analysis of the empty containers was based on the same four ROIs on the acrylic wall as before, to obtain the gradient of GV distribution from the raw 32-bit data. The gradients of the GV curves are the same in each case (2×10^{-6} in terms of GV/slice), showing that the magnitude of the heel effect is not dependent on the overall specimen size. It should be noted that the GV gradients are slightly less than those shown in Figure 8 for the same scan energy. This is because the other scan conditions (power, exposure, resolution) are not identical (Table 3).

5.3 Influence of Soil Grain Size

The potential influence of soil grain size on the heel effect was assessed in dry and wet conditions using the Benchtop machine. Leighton Buzzard sands (Fractions B, C, D and E) and London Clay were used. Dry sand specimens of different grain sizes and wet soil specimens of

Fraction E sand and London Clay were tested separately at two different peak scan energies, 100 kV and 80 kV, respectively (Table 3). A consistent ROI was chosen within each specimen, covering 8 mm of the total 10 mm specimen depth. Global and individual thresholding approaches were used to determine the porosity within the ROI. While it is accepted that thresholding will not be strictly appropriate for the clay specimen owing to the partial volume effect (mean grain size <5µm and scan resolution 9.5µm), the same approach was applied throughout for consistency.

The measured vertical porosity gradients are given in Table 5. The errors induced by the heel effect are quantified by the ratio (Column 6) of the porosity gradients obtained using global (Column 5) and individual (Column 4) thresholding. As individual thresholding is unaffected by the heel effect, this ratio provides a consistent measure of the magnitude of the artefact. The results in Columns 5 and 6 show that the influence of the heel effect increases with decreasing grain size. The effect is apparent in both the dry and the wet specimens, although to a lesser extent in the latter, for a given (smaller) grain size.

The changes in GV gradient (Column 7) for specimens composed of smaller grains are more varied, but there is a clear trend of greater gradients at smaller grain sizes for the same or similar scan energies. The GV gradient for the finer specimens is at least twice that for the coarsest. The data in Table 5 demonstrate that the heel effect is magnified by the thresholding process, particularly when the grain size is small such that it becomes comparable with the spatial resolution.

Table 5: Porosity gradients for different soil grain sizes

Specimen Material	*Comments*	*Featured peak scan energy*	*Porosity Gradient (mm^{-1})*		*Ratio Global: Individual*	*GV Gradient ($\times 10^{-6}$ GV per slice)*
			Individual threshold	*Global threshold*		
Dry LB-B		100 kV	0.416	0.416	1	17.4
Dry LB-C		100 kV	-0.377	-0.842	2.2	45
Dry LB-D		100 kV	-0.120	-0.787	6.6	33.3
Dry LB-E		100 kV	-0.064	-1.797	28.1	51.6
Saturated LB-E		80 kV	-0.483	-1.729	3.58	44.5
Saturated London Clay		80 kV	-0.076	-1.950	25.66	30.6
Dry LB-E	Original Data (Figure 7)	85 kV	-0.1152	-0.9615	8.4	18807
Dry LB-E	Corrected Data (Figure 13)	85 kV	-0.0944	-0.0635	0.7	56

The observed trend is due to two factors. As the grain sizes reduce with respect to the scan resolution, additional errors will be introduced in thresholding owing to the partial volume effect. These errors will be compounded by the heel effect, which increases the underlying apparent GV gradient and hence further impedes the ability of thresholding to resolve the phase proportions accurately. Referring to Figure 6, it can be seen that the heel effect has compressed the GV histogram of a slice near the base of specimen where the image is darkened. This makes thresholding more difficult and will introduce additional errors. For the different grain sizes scanned, the porosity difference over the height of the sample (10mm) due to the heel effect could be over 20%, i.e. an error in excess of ±10%. The systematic nature of this error makes it especially important to identify.

Also included in Table 5 are the porosity gradients from the confirmation scans (the data shown in Figure 7). This case shows a lower global to individual thresholding ratio than the corresponding grain size in the sensitivity analysis, which is to be expected given the better resolution, lower scan energy and other differences in scan settings, but nonetheless the errors are in the same order of magnitude. The differences in scan settings mean that the GV gradient should also not be compared directly with the sensitivity scans, but with the corrected data. The corrected data (discussed in Section 6) show a substantially reduced heel effect, with the artefact eliminated almost entirely. Owing to the use of a different machine (HMX) for these scans, the GV gradients are not directly comparable with the sensitivity scans carried out using the Benchtop machine. Nonetheless the same pattern is shown, with the GV gradient almost eliminated by the correction method.

6 CORRECTION FOR THE HEEL EFFECT

Section 4 has demonstrated the presence of the heel effect in sand and other materials. Section 5 has showed how the effect is influenced by scan energy and the grain size of the soil scanned, and that the heel effect can be of significance in geotechnical problems. The simplest way to avoid the heel effect is to use transmission target CT scanners. This will prevent the introduction of the heel effect into the resulting radiographs. However, depending on available equipment, this option will not always be possible. Therefore two approaches to correcting for the heel effect, and the results of their application, are presented in this Section. First, the role of advanced adaptive thresholding is considered. This could potentially give derived soil phase proportions unaffected by the heel effect, although the original artefact will remain in the CT images and GV data. Secondly, a universal correction technique, termed the “self-wedge”, is proposed. This correction is applied to the radiographic projections directly to provide a completely clean dataset for subsequent analysis.

6.1 Adaptive Thresholding

Adaptive thresholding computes the threshold for each voxel in an image in accordance with GV information from neighbouring voxels. As such, there are similarities to local thresholding and the application of the Otsu method on a slice by slice basis (e.g. the results presented in Section 4.3.2). Adaptive thresholding uses a local area (either circular or rectangular) with the target voxel at its centre. As well as defining the size of this area, several of the more sophisticated approaches (e.g Bernsen, 1986; Niblack, 1986; Phansalskar et al, 2011) also require specification of one or two additional fitting parameters. Owing to the use of local GV information to compute thresholds, adaptive thresholding may only be suitable if there are not expected to be other in situ characteristics or changes within a soil specimen that would be masked by the adaptive process. It also takes longer to carry out than global thresholding.

A number of adaptive thresholding methods were tested using the original HMX scans on Fraction E Leighton Buzzard sand, to see if they could offer a way to overcome the heel effect. Methods based on using adjusted local average GV for the threshold were found to remove the artificial GV gradient induced by the heel effect, but tended to substantially over-estimate the porosity. However, two techniques, one based on local contrast thresholds (Bernsen, 1986) and one that uses the standard deviation as well as the mean in determining the local threshold (Niblack, 1986), were found to work well.

Figure 9 compares the porosity distributions determined using the Otsu method (global thresholding) with those using the adaptive methods of Bernsen (1986) and Niblack (1986). The segmented images using the different approaches are shown in Figure 10. It can be seen that the two adaptive thresholds produce sensible porosity outcomes that are very similar to the individual thresholding using Otsu shown in Figure 7. Furthermore, the average porosities for the two adaptive methods are 38.4 % and 38.6 % respectively, which compares favourably with the Otsu and gravimetric measurement results given in Table 4. This both confirms Otsu as a sensible approach in these types of soils and shows more generally that adaptive thresholding is capable of negating the heel effect.

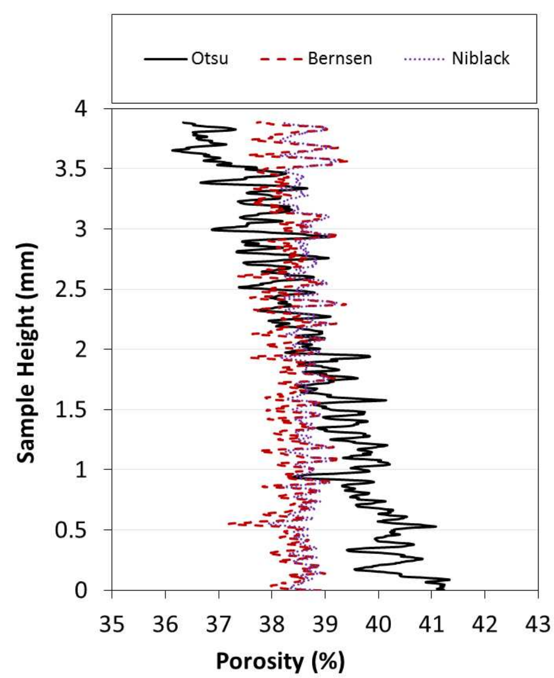

Figure 9: Porosity distributions from the Fraction E Leighton Buzzard sand scanned using the HMX, illustrating the effect of different thresholding methods.

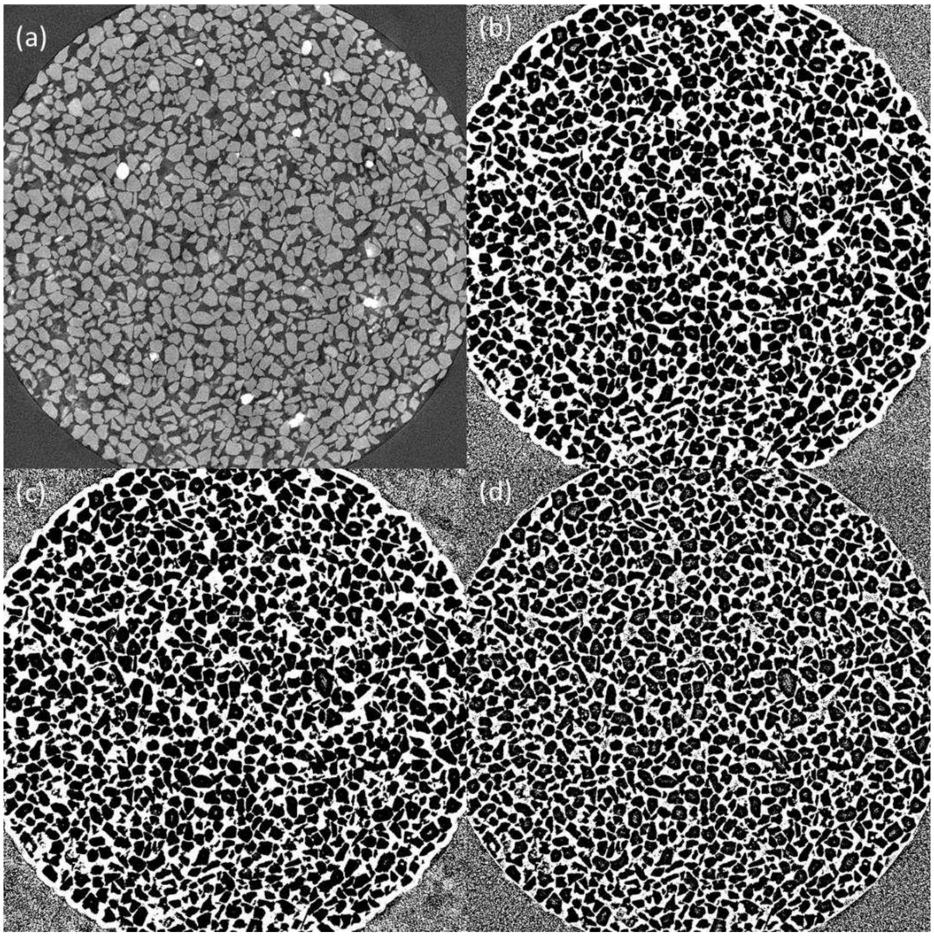

Figure 10: Comparison of images of Fraction E Leighton Buzzard sand from the HMX using different thresholding approaches: (a) original image (b) binarised image using Otsu (individual slice) thresholding (c) Bernsen adaptive thresholding (d) Niblack adaptive thresholding.

However, two other adaptive thresholding methods (Phansalskar et al, 2011; Sauvola & Pietaksinen, 2000) based on the approach of Niblack (1986) were found to underestimate the specimen porosity, despite also removing the artificial GV gradient. This shows that care is always required in selecting thresholding methods and their associated fitting parameters. Given this, it is also desirable to have a universal method for correcting the heel effect, which acts on the original GV data. This will enable the application of global thresholding and implementation of the fullest range of data and image analysis approaches.

6.2 Self-Wedge Correction

6.2.1 Approach

As there are limitations to the use of local and adaptive thresholding methods, a correction to eliminate the errors introduced by the heel effect in the GV data is needed. This will permit the application of a wider range of thresholding and other image processing techniques. Existing correction methods (Section 2.2) may require specific knowledge about the nature of the target, or the placement of compensation filters within the scanner itself. However, a more universal approach would be beneficial in that it could be applied with no special prior knowledge and carried out any time after the scan data had been obtained. The "self-wedge" correction proposed in this paper fulfils this need. It is based on proposals by Ketcham & Carlson (2001) for use with beam hardening. However, application of the technique to the scan data for the 5 mm diameter specimen of Fraction E dry sand in the HMX machine will be the first use of the self-wedge correction for the purpose of countering the heel effect.

The self-wedge correction is based on an X-ray signal calibration method known as a "wedge" (Ketcham & Carlson, 2001), wherein some CT protocols scan a wedge of material of known dimensions or uses the specimen itself (i.e. a "self-wedge") to provide the correction by taking the mean across all projections to calibrate the signal. In this study, the correction method initially averages the 2D radiographic projections for all angles (Figure 11, Step 1). Then the minimum GV in the average projection is subtracted from the averaged projection itself (Figure 11, Step 2), meaning that the average projection, which will be used to correct the original radiographs, has a minimum value of 0. This minimises the deviation from the original grey values.

The process of rotational averaging described above has the potential to introduce artificial ring artefacts. To counter this a median filter is applied (Figure 11, Step 3). A significant kernel size can be applied to the average angular projection, with the kernel size is chosen such that small, high-density artefacts in the mean image can be eliminated. Typically, a kernel value of 5 would suffice, but this may be larger. If a median filter is insufficient then a polar transformation coupled with a Fast Fourier Transform bandpass filter can be applied for the elimination of rings.

The filtered average projection is then subtracted from each original projection in turn (Figure 11, Step 4), ensuring that any grey values falling outside the grey level boundaries are set to that boundary value (for example, if the grey value range is $0 < GV < 65535$, then a value of -3 would be set to 0, a value of 420 would remain at 420, and a value of 65577 would become 65535). If the resulting corrected images appear too dark, it is also possible to scale them at this stage. For subsequent analysis dependent on the absolute grey values, a calibration step can also be included after Step 4 to restore the original grey values. Calibration can be carried out by comparing the corrected image with a single slice from the original, or by a complete Hounsfield unit calibration scan with the same style specimen container (Feeman, 2015).

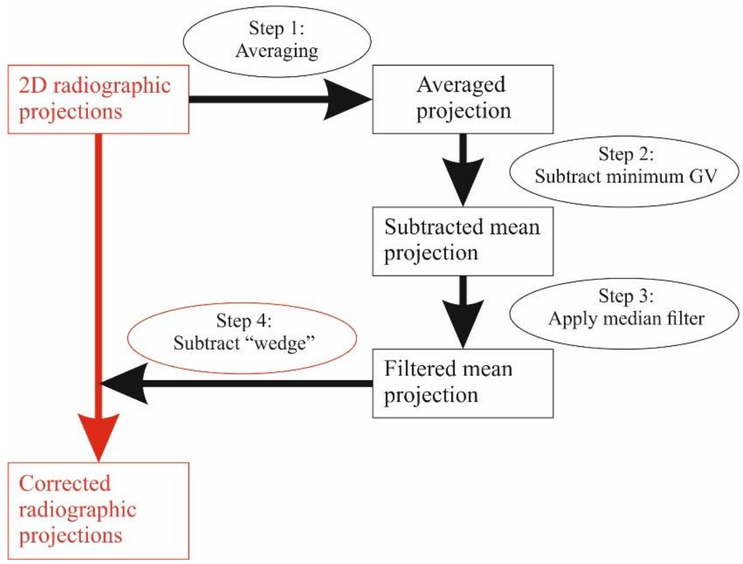

Figure 11: Flowchart for self-wedge correction process

6.2.2 Results

Applying the correction to the 2D projection scan data for the Fraction E dry sand specimen scanned in the HMX results in a small visible change in absolute GV in the reconstructed image data. This is illustrated in Figure 12a and Figure 12c for an orthogonal image. Also shown in Figure 12 are contrast enhanced versions of the images before and after the self-wedge correction. Figure 12b shows the GV gradient resulting from the heel effect, which is absent in the corrected image of Figure 12d.

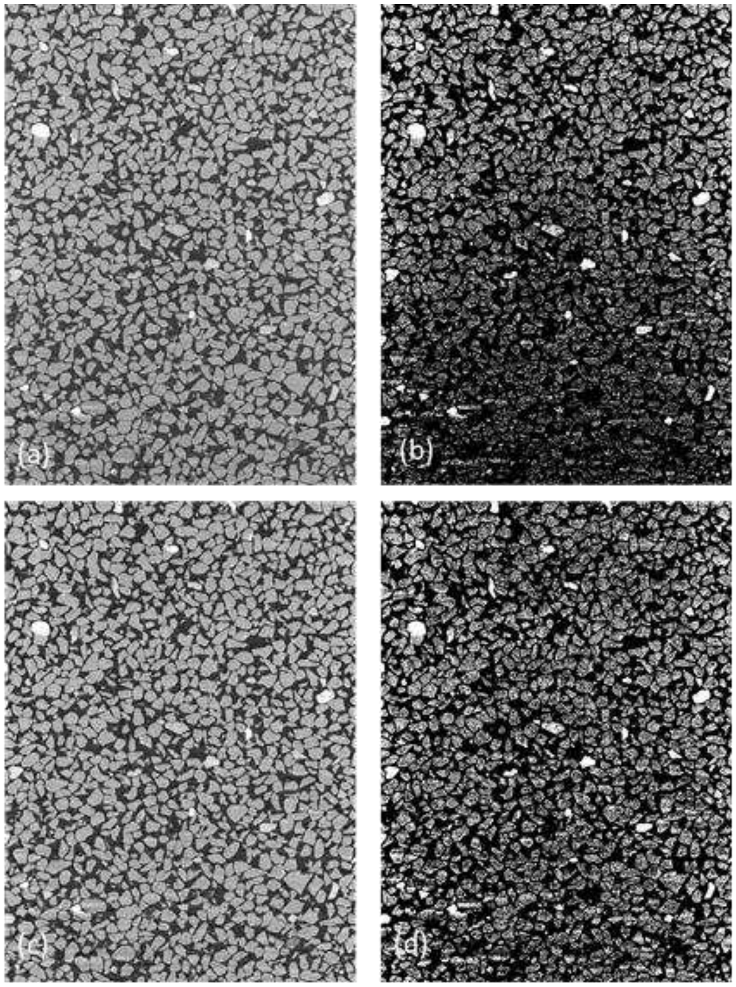

Figure 12: Comparison of orthogonal images; (a) before correction (b) before correction with contrast enhanced (c) after correction (d) after correction with contrast enhanced.

Thresholding was carried out on the HMX data after the self-wedge correction had been applied. Individual and global thresholding of the corrected data using the Otsu method resulted in near identical porosity profiles with negligible heel effect as shown in Table 5. The resulting porosity distribution profiles from global thresholding for the original and corrected data are shown in Figure 13. There is a clear difference between the original and corrected data. The corrected data compare favourably with both the results from the Versa machine (Figure 7), which uses a transmission target, and the local and adaptive thresholding (Figure 9). The overall porosity obtained from the corrected data is unchanged at 38.9 %, which is consistent with the results obtained from the Versa (39.6 %) and gravimetric assessment (39.3 %) shown in Table 4. Thus the self-wedge correction method is shown to have successfully eliminated the heel effect.

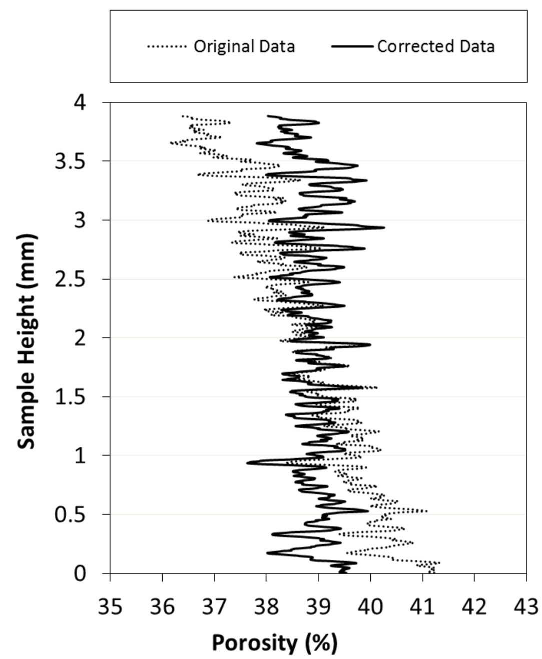

Figure 13: Porosity distributions using global thresholding for the original and weld wedge correct data. Specimen is 5 mm diameter Fraction E Leighton Buzzard dry sand scanned using the HMX machine.

7 SUMMARY AND CONCLUSIONS

The heel effect, an artefact of CT imaging that occurs with scanners using a reflection target for X-ray generation, has been identified in images of soil specimens for the first time. The heel effect results in a gradient in the distribution of the grey value, which is used to determine specimen density, at the detector. Therefore, it may also manifest as an artificial gradient in derived geotechnical parameters such as porosity. Owing to the nature of image reconstruction, the effect will be more significant for reflection targets orientated vertically, and seen especially as a vertical parameter gradient. The heel effect is more significant at high scan energies, hence is relevant to soil mechanics research as this field moves into higher energy temporal scanning; for example for imaging changes in water content or density in response to thermal, chemical or mechanical loading in specimens not in a state of stasis.

The heel effect has been demonstrated to occur in specimens comprising different fractions of Leighton Buzzard sand and London Clay. For a dry Fraction E sand specimen scanned using the HMX machine, the heel effect gave rise to an apparent gradient in porosity, reducing by about 5 % in absolute terms from the top to the bottom of a 4 mm high region, even though the sand specimen was in reality essentially uniform. Subsequent sensitivity scans using the Benchtop machine over a range of grain sizes showed that porosity gradient errors of up to at least ± 10% could be easily generated in a 10 mm high specimen. Thus the heel effect is potentially significant in geotechnical applications of X-ray CT techniques and may give rise to errors, for example in the measurement of the distribution of phase proportions in soils.

It has been shown that specimen size does not significantly influence the heel effect. However for a given scan energy, the soil grain size does. Finer, more densely packed soils are subject to greater heel effect errors, especially when using a thresholding approach for phase determination. The effect will increase in magnitude as the grain size reduces with respect to the scan resolution and the partial volume effect becomes more significant.

To prevent the heel effect entirely reflection targets, especially those orientated vertically, should be avoided. In some circumstances the effect may be negated by the use of local or adaptive thresholding. Alternatively, a simple-to-apply self-wedge correction technique has been developed to remove the error in GV data caused by the heel effect. Corrected HMX porosity profiles compare favourably with those from the Versa machine, which has a transmission target. Importantly, the proposed new correction can be applied universally post-scanning to any data for which the projections are available.

ACKNOWLEDGMENTS

The work reported in this paper forms a part of a project funded by the Royal Academy of Engineering, the Doctoral Training Centre at University of Southampton and EPSRC (EP/G036896/1). The data supporting this study are openly available from the University of Southampton repository (DOI to be confirmed). The authors are also grateful for the contribution of two anonymous reviewers who have helped to improve this publication.

REFERENCES

Alshibli, K. and Hasan, A. (2008) Spatial variation of void ratio and shear band thickness in sand using X-ray computed tomography. Geotechnique, 58 (4), 249-257.

Alvarez-Borges F.J., Richards D.J., Clayton C.R.I., & Ahmed S.I. (2018) Application of X-ray computed tomography to investigate pile penetration mechanisms in chalk. In: Lawrence, J. A et al, Engineering in Chalk. January 2018, 565-570.

Anderson, S., Peyton, R. and Gantzer, C. (1990) Evaluation of constructed and natural soil macropores using X-ray computed tomography. Geoderma, 46 (1-3), 13-29.

Andò, E., Hall, S.A., Viggiani, G., Desrues, J. and Bésuelle, P. (2012a) Experimental micromechanics: grain-scale observation of sand deformation. Géotechnique Letters, 2 (3), 107-112.

Andò, E., Hall, S.A., Viggiani, G., Desrues, J. and Bésuelle, P. (2012b) Grain-scale experimental investigation of localised deformation in sand: a discrete particle tracking approach. Acta Geotechnica, 7 (1), 1-13.

Bernsen, J. (1986). Dynamic thresholding of gray-level images. In Proc. Eighth Int'l conf. Pattern Recognition, Paris.

Boas, F. E. & Fleischmann, D. (2012) CT Artefacts: causes and reduction techniques, Imaging Med, 4 (2), 229 – 240.

Braun, H., Kyriakou, Y., Kachelriess, M. and Kalender, W. (2010) The influence of the heel effect in cone-beam computed tomography: artifacts in standard and novel geometries and their correction. Physics in medicine and biology, 55 (19), 6005.

CíSlerová, M. and Votrubová, J. (2002) CT derived porosity distribution and flow domains. Journal of Hydrology, 267 (3), 186-200.

Cnudde, V. and Boone, M.N. (2013) High-resolution X-ray computed tomography in geosciences: A review of the current technology and applications. Earth-Science Reviews, 123, 1-17.

Davis, G. & Elliott, J. 2006. Artefacts in X-ray microtomography of materials. Materials science and technology, 22(9), 1011-1018.

Desrues, J J M (2004) Tracking strain localization in geomaterials using computerized tomography. Proc. 1st Int. Workshop on X-ray Tomography for Geomaterials. 15-41.

Farber, L., Tardos, G. and Michaels, J.N. (2003) Use of X-ray tomography to study the porosity and morphology of granules. Powder Technology, 132 (1), 57-63.

Feeman, Timothy G. (2010). The Mathematics of Medical Imaging: A Beginner's Guide. Springer Undergraduate Texts in Mathematics and Technology. Springer. ISBN 978-0387927114.

Feldkamp, L., Davis, L. and Kress, J. (1984) Practical cone-beam algorithm. JOSA A, 1 (6), 612-619.

Fonseca, J., O'sullivan, C., Coop, M. and Lee, P. (2013) Quantifying the evolution of soil fabric during shearing using scalar parameters. Géotechnique, 63 (10), 818-829.

Helliwell, J. R., Sturrock, C. J., Grayling, K. M., Tracy, S. R., Flavel, R. J., Young, I. M., Whalley W. R., S. J. Mooney & Mooney, S. J. (2013). Applications of X‐ray computed tomography for examining biophysical interactions and structural development in soil systems: a review. European Journal of Soil Science, 64(3), 279-297.

Hsieh, J., Tang, X., Thibault, J.-B., Shaughnessy, C., Nilsen, R.A. and Williams, E. (2007) Conjugate cone-beam reconstruction algorithm. Optical Engineering, 46 (6), 067001-067001-067010.

Johnston, H., Hilts, M. and Jirasek, A. (2015) Incorporating multislice imaging into x-ray CT polymer gel dosimetry. Medical physics, 42 (4), 1666-1677.

Ketcham, R. A. (2005). Three-dimensional grain fabric measurements using high-resolution X-ray computed tomography. Journal of Structural Geology, 27(7), 1217-1228.

Ketcham, R.A. and Carlson, W.D. (2001) Acquisition, optimization and interpretation of X-ray computed tomographic imagery: applications to the geosciences. Computers & Geosciences, 27 (4), 381-400.

Ketcham, R. A. (2005). Three-dimensional grain fabric measurements using high-resolution X-ray computed tomography. Journal of Structural Geology, 27(7), 1217-1228.
Ketcham, R.A. and Hanna, R.D. (2014) Beam hardening correction for X-ray computed tomography of heterogeneous natural materials. Computers & Geosciences, 67, 49-61.
Khaddour, G., Riedel, I., Andò, E. et al. (2018) Grain-scale characterization of water retention behaviour of sand using X-ray CT. Acta Geotech. 13, 497–512.
King C. (1991) Stratigraphy of the London Clay (Early Eocene) in the Hampshire Basin. PhD Thesis, Kingstone Polytechnic.
Liu, K. (2020) Computed Tomography (CT) Scanning to Quantify the Movement of Moisture in Soils under Thermal Gradients. EngD thesis, University of Southampton.
Liu, K., Loveridge, F.A., Boardman, R. and Powrie, W. (2017) Study of Short-term Evaporation in Sand Specimens via Micro-focus X-ray Computed Tomography. Paper presented at 2nd International Symposium on Coupled Phenomena in Environmental Geotechnics (CPEG2), Leeds, UK.
Mees, F., Swennen, R., Van Geet, M., & Jacobs, P. (2003). Applications of X-ray computed tomography in the geosciences. Geological Society, London, Special Publications, 215(1), 1-6.
Niblack, W. (1986). An Introduction to Digital Image Processing, 115–116 Prentice-Hall. Englewood Cliffs, New Jersey.
Mori, S., Endo, M., Nishizawa, K., Ohno, M., Miyazaki, H., Tsujita, K. and Saito, Y. (2005) Prototype heel effect compensation filter for cone-beam CT. Physics in medicine and biology, 50 (22), N359.
Otani, J., Watanabe, Y. & Chevalier, B. (2010) Introduction of X-ray CT application in geotechnical engineering – theory and practice, IOP Conf. Series: Materials Science and Engineering 10 (2010) 012089 doi:10.1088/1757-899X/10/1/012089.
Otsu, N. (1979) A threshold selection method from gray-level histograms. IEEE transactions on systems, man, and cybernetics, 9 (1), 62-66.
Phansalskar, N, More, S, Sabale, A & Joshi, M. (2011), Adaptive local thresholding for detection of nuclei in diversity stained cytology images, International Conference on Communications and Signal Processing (ICCSP): 218-220.
Taud, H., Martinez-Angeles, R., Parrot, J. and Hernandez-Escobedo, L. (2005) Porosity estimation method by X-ray computed tomography. Journal of petroleum science and engineering, 47 (3), 209-217.
Sauvola, J & Pietaksinen, M (2000), Adaptive Document Image Binarization, Pattern Recognition 33(2): 225-236.
Sleutel, S., Cnudde, V., Masschaele, B., Vlassenbroek, J., Dierick, M., Van Hoorebeke, L., Jacobs, P. and De Neve, S. (2008) Comparison of different nano-and micro-focus X-ray computed tomography set-ups for the visualization of the soil microstructure and soil organic matter. Computers & Geosciences, 34 (8), 931-938.
Swinehart, D. F. (1962). The beer-lambert law. Journal of chemical education, 39(7), 333-335.

University of Southampton (2017) μ-VIS: Multidisciplinary, Multiscale, Microtomographic Volume Imaging. Available from: http://www.southampton.ac.uk/muvis/about/index.page [Accessed 20th November 2019].

Van Geet, M., Swennen, R., & Wevers, M. (2000). Quantitative analysis of reservoir rocks by microfocus X-ray computerised tomography. Sedimentary Geology, 132(1-2), 25-36.

J.-P. Wang, E. Andò, P. Charrier, S. Salager, P. Lambert, and B. François (2019) Micro-scale investigation of unsaturated sand in mini-triaxial shearing using X-ray CT, Géotechnique Letters, 9:4, 269-277

Watanabe, Y., Lenoir, N., Otani, J., & Nakai, T. (2012). Displacement in sand under triaxial compression by tracking soil particles on X-ray CT data. Soils and foundations, 52(2), 312-320.

Zhang, X., Mavroulidou, M. & Gunn, M.J. (2016) A study of the water retention curve of lime-treated London Clay, Acta Geotech. 12 (1), 23-45.

Zhao, B., Wang, J., Coop, M., Viggiani, G. and Jiang, M. (2015) An investigation of single sand particle fracture using X-ray micro-tomography. Géotechnique, 65 (8), 625-641.

Zbijewski, W. and Beekman, F.J. (2006) Efficient Monte Carlo based scatter artifact reduction in cone-beam micro-CT. Medical Imaging, IEEE Transactions on, 25 (7), 817-827.

List of Figures and Tables

Table 1: Grain Sizes of Soil Materials

Table 2: Features of various scanners (see University of Southampton (2017) for more details)

Table 3: Experiment Details and Scan Settings

Table 4: Overall porosity from HMX and Versa scans of a 5 mm diameter dry Fraction E Leighton Buzzard sand specimen

Table 5: Porosity gradients for different soil grain sizes